Recurrent De Novo and Biallelic Variation of *ATAD3A*, Encoding a Mitochondrial Membrane Protein, Results in Distinct Neurological Syndromes

Tamar Harel,[1,31,*] Wan Hee Yoon,[2,3,31] Caterina Garone,[4] Shen Gu,[1] Zeynep Coban-Akdemir,[1] Mohammad K. Eldomery,[1] Jennifer E. Posey,[1] Shalini N. Jhangiani,[1,5] Jill A. Rosenfeld,[1,6] Megan T. Cho,[7] Stephanie Fox,[8] Marjorie Withers,[1] Stephanie M. Brooks,[9] Theodore Chiang,[5] Lita Duraine,[2,3] Serkan Erdin,[10,11] Bo Yuan,[1,6] Yunru Shao,[1] Elie Moussallem,[1] Costanza Lamperti,[12] Maria A. Donati,[13] Joshua D. Smith,[14] Heather M. McLaughlin,[7] Christine M. Eng,[1,6] Magdalena Walkiewicz,[1,6] Fan Xia,[1,6] Tommaso Pippucci,[15] Pamela Magini,[16] Marco Seri,[15,16] Massimo Zeviani,[12] Michio Hirano,[17] Jill V. Hunter,[18] Myriam Srour,[19] Stefano Zanigni,[20,21] Richard Alan Lewis,[1,22,23] Donna M. Muzny,[5] Timothy E. Lotze,[23,24] Eric Boerwinkle,[5,25] Baylor-Hopkins Center for Mendelian Genomics, University of Washington Center for Mendelian Genomics, Richard A. Gibbs,[1,5] Scott E. Hickey,[9] Brett H. Graham,[1] Yaping Yang,[1,6] Daniela Buhas,[8,26] Donna M. Martin,[27,28] Lorraine Potocki,[1,23] Claudio Graziano,[15] Hugo J. Bellen,[1,2,3,29,30] and James R. Lupski[1,5,22,23,*]

ATPase family AAA-domain containing protein 3A (ATAD3A) is a nuclear-encoded mitochondrial membrane protein implicated in mitochondrial dynamics, nucleoid organization, protein translation, cell growth, and cholesterol metabolism. We identified a recurrent de novo *ATAD3A* c.1582C>T (p.Arg528Trp) variant by whole-exome sequencing (WES) in five unrelated individuals with a core phenotype of global developmental delay, hypotonia, optic atrophy, axonal neuropathy, and hypertrophic cardiomyopathy. We also describe two families with biallelic variants in *ATAD3A*, including a homozygous variant in two siblings, and biallelic *ATAD3A* deletions mediated by nonallelic homologous recombination (NAHR) between *ATAD3A* and gene family members *ATAD3B* and *ATAD3C*. Tissue-specific over-expression of *bor*[R534W], the *Drosophila* mutation homologous to the human c.1582C>T (p.Arg528Trp) variant, resulted in a dramatic decrease in mitochondrial content, aberrant mitochondrial morphology, and increased autophagy. Homozygous null *bor* larvae showed a significant decrease of mitochondria, while overexpression of *bor*[WT] resulted in larger, elongated mitochondria. Finally, fibroblasts of an affected individual exhibited increased mitophagy. We conclude that the p.Arg528Trp variant functions through a dominant-negative mechanism that results in small mitochondria that trigger mitophagy, resulting in a reduction in mitochondrial content. *ATAD3A* variation represents an additional link between mitochondrial dynamics and recognizable neurological syndromes, as seen with *MFN2*, *OPA1*, *DNM1L*, and *STAT2* mutations.

Introduction

Remodeling of the mitochondrial membrane through continuous cycles of fusion and fission promotes mixing of mitochondrial proteins and DNA, ensuring proper func-tion.[1–3] Pathogenic variation in genes encoding fusion and fission factors, including *MFN2* (MIM: 608507),[4–7] *OPA1* (MIM: 605290),[8,9] *DNM1L* (MIM: 603850),[10,11] *STAT2* (MIM: 600556),[12] *SLC25A46* (MIM: 610826),[13] and *GDAP1* (MIM: 606598)[14] have been associated with

[1]Department of Molecular and Human Genetics, Baylor College of Medicine, Houston, TX 77030, USA; [2]Department of Molecular and Human Genetics, Jan and Dan Duncan Neurological Research Institute, Baylor College of Medicine, Houston, TX 77030, USA; [3]Howard Hughes Medical Institute, Jan and Dan Duncan Neurological Research Institute, Baylor College of Medicine, Houston, TX 77030, USA; [4]MRC Mitochondrial Biology Unit, Cambridge CB2 0XY, UK; [5]Human Genome Sequencing Center, Baylor College of Medicine, Houston, TX 77030, USA; [6]Baylor Genetics, Baylor College of Medicine, Houston, TX 77030, USA; [7]GeneDx, Gaithersburg, MD 20877, USA; [8]Medical Genetics Department, Montreal Children's Hospital, Montreal, QC H4A 3J1, Canada; [9]Department of Pediatrics, The Ohio State University College of Medicine, Division of Molecular and Human Genetics, Nationwide Children's Hospital, Columbus, OH 43205, USA; [10]Center for Human Genetic Research, Massachusetts General Hospital, Boston, MA 02114, USA; [11]Program in Medical and Population Genetics, Broad Institute of MIT and Harvard, Cambridge, MA 02142, USA; [12]Unit of Molecular Neurogenetics, The Foundation "Carlo Besta" Institute of Neurology-IRCCS, Milan 20126, Italy; [13]Metabolic and Muscular Unit, Meyer Children's Hospital, University of Florence, Florence 50132, Italy; [14]Department of Genome Sciences, University of Washington, Seattle, WA 98195, USA; [15]Medical Genetics Unit, Policlinico Sant'Orsola-Malpighi, University of Bologna, Bologna 40138, Italy; [16]Medical Genetics Unit, Department of Medical and Surgical Science, University of Bologna, Bologna 40138, Italy; [17]Department of Neurology, Columbia University Medical Center, New York, NY 10032, USA; [18]Department of Pediatric Radiology, Texas Children's Hospital, Houston, TX 77030, USA; [19]Department of Pediatrics, Neurology and Neurosurgery, McGill University, Montreal, QC H4A 3J1, Canada; [20]Functional MR Unit, Policlinico S. Orsola - Malpighi, Bologna 40138, Italy; [21]Department of Biomedical and Neuromotor Sciences (DIBINEM), University of Bologna, Bologna 40123, Italy; [22]Department of Pediatrics, Baylor College of Medicine, Houston, TX 77030, USA; [23]Texas Children's Hospital, Houston, TX 77030, USA; [24]Department of Pediatric Neurology, Texas Children's Hospital, Houston, TX 77030, USA; [25]Human Genetics Center, The University of Texas Health Science Center, Houston, TX 77030, USA; [26]Human Genetics Department, McGill University, Montreal, QC H3A 0G4, Canada; [27]Department of Pediatrics and Communicable Diseases, University of Michigan, Ann Arbor, MI, 48109; [28]Department of Human Genetics, University of Michigan, Ann Arbor, MI 48109, USA; [29]Program in Developmental Biology, Jan and Dan Duncan Neurological Research Institute, Baylor College of Medicine, Houston, TX 77030, USA; [30]Department of Neuroscience, Jan and Dan Duncan Neurological Research Institute, Baylor College of Medicine, Houston, TX 77030, USA
[31]These authors contributed equally to this work
*Correspondence: harel.tamar@gmail.com (T.H.), jlupski@bcm.edu (J.R.L.)
http://dx.doi.org/10.1016/j.ajhg.2016.08.007.

recognizable human syndromes including optic atrophy, peripheral neuropathy, cardiomyopathy, brain malformations, and developmental delay as recurrent features.

ATAD3A (MIM: 612316) is ubiquitously expressed and encodes an ATPase family AAA-domain containing protein 3A (ATAD3A) that simultaneously interacts with the outer and inner mitochondrial membranes. In vitro studies show that ATAD3A is involved in diverse cellular processes, including mitochondrial dynamics,[15] mitochondrial DNA (mtDNA) maintenance and replication,[16] channeling of cholesterol for steroidogenesis,[17,18] and resistance of cancer cells to therapy.[19,20] Co-immunoprecipitation in lung adenocarcinoma cell lines revealed evidence for interaction of ATAD3A with MFN2, OPA1, and DNM1L,[21] suggesting that ATAD3A may affect mitochondrial dynamics via interaction with these proteins.

The ATAD3 gene family in humans includes three paralogs (*ATAD3A*, *ATAD3B* [MIM: 612317], and *ATAD3C*) positioned in tandem on chromosome 1p36.33 and appears to have recently evolved by duplication of a single ancestral gene.[22,23] Disruption of the *Drosophila* ortholog (*bor*), which has ~70% similarity to human *ATAD3A*, results in growth arrest during larval development.[15] The ortholog in *C. elegans* is essential for mitochondrial activity and development.[24] *Atad3* homozygous null mice are embryonic lethal at day E7.5 due to growth retardation and defective development of the trophoblast lineage, whereas heterozygotes for a loss-of-function allele seem unaffected.[22] RNAi studies of ATAD3A in HeLa and lung cancer cells have documented increased mitochondrial fragmentation and a decreased co-localization of mitochondria and endoplasmic reticulum (ER).[21] Despite multiple studies in vitro and in animal models, the precise function of ATAD3A has not been elucidated to date.

We identified an identical de novo heterozygous variant in *ATAD3A* in five individuals. In addition, we identified two families with biallelic single-nucleotide variants (SNVs) or copy-number variants (CNVs) involving *ATAD3A*. Our data indicate that both monoallelic and biallelic pathogenic variation in *ATAD3A* led to the observed neurological phenotypes in these seven families. Functional studies in fibroblasts from an affected individual and in *D. melanogaster* revealed significant mitochondrial abnormalities and indicate that ATAD3A is required to maintain the proper size and number of mitochondria in neurons and muscles.

Material and Methods

Subjects

Families 1, 2, 3, 5, and 7 provided consent according to the Baylor-Hopkins Center for Mendelian Genomics (BHCMG) research protocol H-29697, approved by the Institutional Review Board (IRB) at Baylor College of Medicine (BCM). Families 4 and 6 provided consent according to protocol M0010, approved by the IRB at Meyer Children Hospital, Florence, and protocol 13084, approved by the IRB at AUSL, Bologna, respectively. Subjects are described further in Tables 1 and S1.

Whole-Exome Sequencing

Family 1, II-2 (proband), family 5 (parents and proband), and family 7 (proband) had whole-exome sequencing (WES) at Baylor Genetics (BG, BCM) according to the protocol described in Yang et al.[25] After clinical WES results were unrevealing for a potential etiologic molecular diagnosis in known disease genes, parental exome sequencing for family 1 was obtained through the BHCMG research initiative. In brief, DNA samples were prepared into Illumina paired-end libraries and underwent whole-exome capture with the BCM-HGSC core design (52 Mb, Roche NimbleGen), followed by sequencing on the Illumina HiSeq 2000 platform (Illumina). Data produced were aligned and mapped to the human genome reference sequence (hg19) by the Mercury pipeline.[26] Single-nucleotide variants (SNVs) were called with the ATLAS (an integrative variant analysis pipeline optimized for variant discovery) variant calling method and annotated by the in-house-developed "Cassandra" annotation pipeline that uses ANNOVAR (Annotation of Genetic Variants) and additional tools and databases.[27–29] De novo variants were calculated by an in-house developed pipeline (DNM-Finder) for in silico subtraction of parental variants from the proband's variants in vcf files while accounting for the read number information extracted from BAM files. Bioinformatic tools predicted conservation and pathogenicity of candidate variants, and variants were compared against both an internal database (~5,000 exomes) and publicly available databases such as the 1000 Genomes Project, the Exome variant server, NHLBI GO Exome Sequencing Project (ESP), the Atherosclerosis Risk in Communities Study (ARIC) Database, and the Exome Aggregation Consortium (ExAC) database. Families 5 and 7 were identified through an internal database. The GeneMatcher tool facilitated identification of four additional families with variants of interest in *ATAD3A*.[30] Detailed sequencing methods for these families can be found in the Supplemental Data.

PCR Amplification and Sanger Sequencing

An amplicon containing the *ATAD3A* variant was amplified from genomic DNA by conventional PCR, with a primer design that ensured specific amplification of *ATAD3A* and not its homolog *ATAD3B*. Representative primers for family 1, II-2 were ATAD3A-F1 (5′-CCC CTC CAA AGA GGA TGT TT-3′) and ATAD3A-R1 (5′-CAA CTG AGC ATC TCC ACA GC-3′). Additionally, the homologous exon of *ATAD3B* was sequenced with a specific intronic primer: ATAD3B-F1 (5′-TGC CTC ACT TGG GAA CTC C-3′) and ATAD3B-R1 (5′-ACA GAA GCT CCC ACA TGA CA-3′). PCR products were purified by ExoSAP-IT (Affymetrix) and analyzed by standard Sanger di-deoxy nucleotide sequencing (DNA Sequencing Core Facility, Baylor College of Medicine). Details for Sanger validation and segregation of variants in other individuals can be found in the Supplemental Data.

3D Modeling of Protein Structure

The 3D protein structure model of ATAD3A (GenBank: NM_001170535.1) was predicted by I-TASSER.[31,32] The side chain orientation of the mutant residue was obtained by the PyMol Molecular Graphics System, v.1.5 Schrodinger, LLC. Amino acid conservation was obtained from the Consurf server based on sequence analysis.[33]

Biochemistry

The activities of mitochondrial respiratory chain complexes (I-IV) and Citrate Synthase (CS) were measured in skeletal muscle

Table 1. Comparison of the Phenotypic Features of Seven Individuals with *ATAD3A* Variants

	Monoallelic					Biallelic		
	Family 1, II-2	Family 2, II-4	Family 3, II-1	Family 4, II-1	Family 5, II-1	Family 6, II-1	Family 6, II-2	Family 7, II-1
Age at last exam	9 years	5 years	3 years	5 years	23 months	26 years	24 years	5 days
Gender	F	F	M	F	M	F	M	F
DD	+	+	+	+	+	+	+	NR
ID	+ (mild)	+	+	+	+	+ (mild)	−	NR
Seizures	−	−	−	−	−	+	+	+
Optic atrophy	+	−	+	+	−	−	−	−
Congenital cataract	−	−	−	−	−	+	+	−
Corneal clouding	−	−	−	−	−	−	−	+
Hypotonia	+	+	+	+	+	+	+	+
Spasticity	+	+	+	+	−	−	−	+
Pectus carinatum	−	−	+	−	−	−	+	−
Peripheral neuropathy	+	+	+	+	borderline	−	−	NR
Hypertrophic cardiomyopathy	−	−	+	+	−	−	−	mild RVH with septal hypertrophy (newborn)
Elevated plasma lactate	−	+ (mild)	+ (intermittent)	+	NR	NR	+	NR
Cerebellar atrophy/ hypoplasia	−	−	−	−	−	+ (moderate)	+ (mild)	+ (severe)
MR spectroscopy	normal	NR	lactate peak	NR	NR	reduction of left cerebellar hemisphere NAA	normal	reduction of NAA, increased choline
Other	ADHD	deficiency complex I+III	methyl-glutaconic aciduria; growth hormone deficiency; dystonia	methyl-glutaconic aciduria; deficiency complex II+III, II+CS	47,XXY	delayed puberty, hyposomia	delayed puberty, delayed bone age, hyposomia, cryptorchidism	smooth sulcal/gyral pattern, hypoplasia of posterior fossa structures, intubated at birth; deceased at 13 days

Abbreviations are as follows: ADHD, attention deficit hyperactivity disorder; CS, citrate synthase; DD, developmental delay; F, female; ID, intellectual disability; IQ, intelligence quotient; M, male; MR, magnetic resonance; NAA, N-acetyl aspartate; NR, not reported; RVH, right ventricular hypertrophy.

homogenates and digitonin-treated cultured skin fibroblasts as described previously.[34] Activities are expressed relative to CS for the muscle or relative to mitochondrial protein for fibroblasts.

Detection of CNV from WES Read Depth Analysis

Internal databases were screened for homozygous CNVs using two in-house-developed algorithms. The first method utilized a dual normalization approach consisting of principal component analysis (PCA)-XHMM[35] intermediates and read per kilobase per million mapped reads (RPKM). The former normalized raw read depth values with PCA, which were then centered by exon target on a Z-score scale, whereas the latter was normalized at the sample level (RPKM). The intersection of two orthogonal normalization approaches (target based and sample based) allowed for an enhancement in signal and reduction in noise. In each method, we removed exons with extreme GC content and low complexity biases from analysis. Regions with either very high or very low GC content are more likely to be captured poorly by WES. Complete homozygous and hemizygous exon deletions were called by strict filtering criteria, including exon target Z-scores less than -2 and RPKM equal or near 0. The second algorithm, in the R programming language, was also based on the total number of reads (TR) in each exon and normalized read depth values (RPKM).

High-Density Array Comparative Genomic Hybridization

To further characterize the CNVs involving the *ATAD3A* genomic region, we designed an 8× 60K oligonucleotide array with ~200 bp per probe spacing from Agilent Technologies (AMADID 082882). DNA from HapMap individual NA15510 was used as hybridization control. Scanned array images were processed using Agilent Feature Extraction software (v.10) and extracted files were analyzed using Agilent Genomic Workbench (v.7.0.4.0). Array designs and sequence alignment for breakpoint analysis were based on the February 2009 genome build (GRCh37/hg19 assembly).

Evaluation of CNV Boundaries and Breakpoint Junction Analysis

Droplet digital PCR (ddPCR) was performed using the QX200 AutoDG Droplet Digital PCR System from Bio-Rad according to manufacturer's protocols. In brief, a 20 μL mixture was set up for each PCR reaction, containing 10 μL of 2× Q200 ddPCR EvaGreen Supermix, 0.25 μL of each primer (10 μM) and 20 ng of genomic DNA. Reaction mixture was subjected to automatic droplet generation, followed by PCR reaction and droplet reading. Cycling conditions for PCR were as follows: 5 min at 95°C, 40 cycles of 30 s at 95°C/1 min at 67.1°C/1 min at 72°C, 5 min at 4°C, 5 min at 90°C and final hold at 4°C. Ramp rate was set for 2°C per s for all steps. Data were analyzed with QuantaSoft Software (Bio-Rad), and concentrations of positive droplets (number of positive droplets per μL of reaction) were obtained for each PCR reaction. Raw data of ddPCR and primer sequences are shown as Table S2.

The breakpoint junctions were amplified with either TaKaRa LA Taq (Clontech) or QIAGEN HotStarTaq DNA Polymerase according to the manufacturer's protocol. The breakpoint junction of BAB8733 (family 7, II-2) was amplified with the following primers: BAB8733_del_F1 (5′-TTG GAG TTC TGT GGT CCT GG-3′) and BAB8733_del_R1 (5′-CAG GCC CAC ACT GCT GAC-3′), while the wild-type allele was amplified with BAB8733_wt_F2 (5′-ATG GGC ACA GTC ACA GGT TT-3′) and BAB8733_del_R1. The breakpoint junction of BAB8734 (family 7, II-1) was amplified with the primers BAB8734_del_F3 (5′-GAG AGC GGA GTC CAC ACC-3′) and BAB8734_del_R3 (5′-GGA AAC CAA CCA CAC ACG G-3′), while the wild-type allele was amplified with BAB8734_del_F3 and BAB8734_wt_R4 (5′-CTG ATC CAC CGA CAG AAG CAG-3′).

Miropeats

The Miropeats program descriptively illustrates the genomic architecture by plotting the intra-species alignments of the reference genome. ICAass (v.2.5) algorithm performed DNA sequence comparisons, and Miropeats (v.2.01) was then applied for converting the comparisons into graphical display based on the position and matching quality.[36] A threshold of 200 was set for comparison of human paralogs.

Fly Strains and Maintenance

The following stocks were obtained from the Bloomington Stock Center at Indiana University (BDSC):

w[1118]; PBac{PB}bor[c05496]/TM6B, Tb[1]
w[1118]; Df(3R)Exel7329/TM6B, Tb[137]
y[1] w*; tubulin-Gal4/*TM3, Sb[1] Ser[1]*
w*; *Ubi-Gal4 /CyO*
yw;+; n-syb-Gal4
w; D42-Gal4 UAS-mito-HA-GFP e/TM6B, Tb (from Bill Saxton)
w; *C57-Gal4*

All flies were maintained at room temperature (21°C). All crosses were kept at 21°C except those for *C57-Gal4* (25°C).

Cloning and Transgenesis

LD30988, an EST of *bor* (Drosophila Genomics Resource Center), contains a mutation that causes a substitution of an amino acid (D40 to Y) and an insertion of 72 additional nucleotides near the 3′ end. These mutations were corrected by site-directed PCR using primers bor Y40→D-F (5′-acg gcc ggc gag aag tcc ggg Gat tcg caa ctg agc cgg gcg-3′) and bor Y40→D-R (5′-cgc ccg gct cag ttg cga atC ccc gga ctt ctc gcc ggc cgt-3′); LD30988-F (5′-CAG CCT GCC GCT GCG GGT GCC AAG cgg ttc aaa ctg gac acc ttt gat-3′) and LD30988-R (5′-atc aaa ggt gtc cag ttt gaa ccg CTT GGC ACC CGC AGC GGC AGG CTG-3′). All final clones were confirmed by sequencing.

To generate *bor* p.Arg534Trp (R534W) (equivalent to human p.Arg528Trp), we performed site-directed mutagenesis using primers 5′-ctg tgc gag ggt atg tcg ggt TgG gaa atc tcc aag ctg ggc-3′ and 5′-gcc cag ctt gga gat ttc CcA acc cga cat acc ctc gca cag-3′. The corrected *bor* EST clone and *bor* (R534W) clone were amplified by PCR using primers bor-F BamHI (5′-cat ttt GGA TCC aaa ATG TCG TGG CTT TTG GGC AGG-3′) and bor-R NotI (5′-tgt aaG CGG CCG CTT ACA GTT TCT TTG CAG TTA G-3′). The PCR products were subcloned into BglII/NotI sites in a pUASTattB[38] vector to generate pUASTattB-bor[WT] and pUASTattB-bor[R534W]. The pUASTattB constructs were injected into *y,w,ΦC31; VK37* embryos[39] and transgenic flies were selected.

Larvae Dissection and Immunostaining

For muscle and axon staining, third instar larvae were dissected as described in Bellen and Budnik.[40] In brief, third instar larvae were fixed in 4% formaldehyde for 30 min at room temperature, rinsed in PBS twice, and washed in PBS containing 0.3% Triton X-100 three times. The primary antibodies were used at the following dilutions: mouse anti-ATP5A 1:500 (abcam), chick anti-GFP 1:1,000 (abcam), mouse anti-Dlg 1:250 (mAb 4F3, DSHB; developed by C.S.

Goodman, Renovis), and rabbit anti-HRP 1:1,000 (Jackson ImmunoResearch). Alexa 488-conjugated (Invitrogen) and Cy3- or Cy5-conjugated secondary antibodies (Jackson ImmunoResearch) were used at 1:120. Samples were mounted in Vectashield (Vector Labs). Alexa Fluor 568 phalloidin (ThermoFisher) was used at 1:1,000.

Bright-Field Imaging and Transmission Electron Microscopy of Flies

Drosophila larval muscles and neuro-muscular junctions (NMJs) were imaged according to standard electron microscopy procedures using a Ted Pella Bio Wave processing microwave with vacuum attachments. In brief, whole first instar larvae were dissected at room temperature under modified Karnovski's fixative consisting of 2% paraformaldehyde, 2.5% glutaraldehyde, in 0.1 M sodium cacodylate buffer at pH 7.2. The NMJ muscle samples were filleted under modified Karnovski's fixative and allowed to sit pinned under fixative for 40 min. After dissection the first instar larvae and NMJs were fixed for 2 days in fresh modified Karnovski's fixative rotating in a 4°C cold room. After 2 days in fixative, the samples were irradiated using the Ted Pella Biowave Microwave, rinsed three times with Millipore water, post-fixed with 1% aqueous Osmium Tetroxide, and rinsed again three times with Millipore water.

Concentrations from 30%–100% of ethanol were used for the initial dehydration series, followed with propylene oxide as the final dehydrant. The samples were gradually infiltrated with 3 ratios of propylene oxide and Embed 812, finally going into three changes of pure resin all under vacuum. Samples were allowed to infiltrate in pure resin overnight on a rotator. The samples were embedded into flat silicone molds and cured in the oven at 62°C for 3 days. The polymerized samples were thin-sectioned at 50 nm and stained with 1% uranyl acetate for 12 min followed by lead citrate for 2 min before TEM examination. Grids were viewed in a JEOL 1400 Plus transmission electron microscope at 80 kV. Micrographs were captured by an AMT XR-16 mid-mount 16 mega-pixel digital camera.

Fibroblast Culture and TEM

Human fibroblasts were grown in DMEM (10569-010, Life Technologies) supplemented with 10% fetal bovine serum (FBS) and penicillin-streptomycin (Sigma) at 37°C. For fixation, cells were placed in a 50:50 media/fix solution with Karnovski's fixative (2% paraformaldehyde and 2.5% glutaraldehyde in 1% sodium cacodylate buffer) for 10 min, followed by 100% Karnovski's fixative for 45 min. Cells were scraped and placed into micro-centrifuge tubes, spun down at 1,500 × *g* for 3 min, and left in fresh fixative for 15 min after an additional centrifugation. The cell pellets were then subjected to a normal processing procedure as above.

Immunoblotting Analysis

Protein concentration was quantitated using the Bio-Rad DC protein assay. 10 μg of total lysate or DDM-treated crude mitochondria protein were analyzed by electrophoresis in NuPage Novex 4%–12% bis-tris gel (Invitrogen). After electrophoresis, proteins were transferred electrophoretically to a PVDF membrane and probed with the following antibodies: rabbit polyclonal anti-ATAD3A (1:1,000, Novus Biological), anti-GAPDH (1:10,000, Abcam), or anti-VDAC1 (1:10,000, Abcam). HRP-conjugated anti-rabbit or anti-mouse IgG secondary antibodies (Promega) were used at a dilution of 1:3,000. The protein bands were visualized by chemiluminescence, using reagents purchased from GE Healthcare.

Results

De Novo *ATAD3A* Variant Is Associated with Optic Atrophy and Peripheral Neuropathy

The clinical findings of five affected individuals from five families with an identical, recurrent de novo variant in *ATAD3A* (g.chr1:1464679C>T [hg19]; GenBank: NM_001170535.1; c.1582C>T [p.Arg528Trp], Figures 1 and S1–S4) are summarized in Tables 1 and S1; detailed case reports can be found in the Supplemental Data and photographs are available in Figure 2. The phenotypic spectrum included developmental delay (5/5), hypotonia (5/5), optic atrophy (3/5), peripheral neuropathy (4/5), and hypertrophic cardiomyopathy (2/5). Mitochondrial dysfunction was suggested in different cases by intermittently or mildly elevated plasma lactate, a lactate peak on MR spectroscopy, slightly increased excretion of 3-methylglutaconic acid, and/or deficiency in respiratory chain activities on muscle homogenate (Supplemental Data). These phenotypic features bear striking resemblance to those encountered with pathogenic variation in other mitochondrial fission and fusion proteins, including *DNM1L*,[10,11] *MFN2*,[5,7] *OPA1*,[8,9] and *SLC25A46*[13] (Figure S5).

The c.1582C>T variant has robust bioinformatic damaging predictions (Table S3), arose at a CpG dinucleotide (Figure 1B),[41–43] and was absent from internal and publicly available databases, including the ExAC database of ~60,000 unrelated individuals. 3D structural modeling further supported pathogenicity, as the long side chain of arginine at position 528 is replaced by the flat aromatic ring of tryptophan and alters the configuration of a conserved pocket, possibly a functional site (Figure 1D). To ensure that the variant was specific to *ATAD3A* and to investigate the possibility of gene conversion from the highly homologous *ATAD3B*, primer design was targeted to specific intronic sequences flanking the exon. No variation was seen in *ATAD3B*, suggesting that the c.1582C>T variant is specific to *ATAD3A*. This argues against gene conversion as a mutational mechanism (Figure S1).

Sanger sequencing of the maternal sample in family 4 suggested low-level mosaicism in genomic DNA derived from blood (Figure S3). Nerve conduction velocities of the mother (family 4, I-2) were within normal range; however, she had cardiac arrhythmia diagnosed in childhood and required a pacemaker, which might be a clinical phenotype relevant to the *ATAD3A* variation given the cardiac phenotype in two individuals with the recurrent de novo variant and our inability to assess the degree of mosaicism in the mother's heart tissue. The proband in family 5 had a dual molecular diagnosis, including Klinefelter syndrome and the *ATAD3A* variant. Dual molecular diagnoses have been documented in ~4.6%–7.2% of molecularly diagnosed individuals.[25,44–46] Both of these clinical situations, parental mosaicism and dual molecular diagnoses, require specific consideration with respect to prognosis and recurrence risk for the families.[47,48]
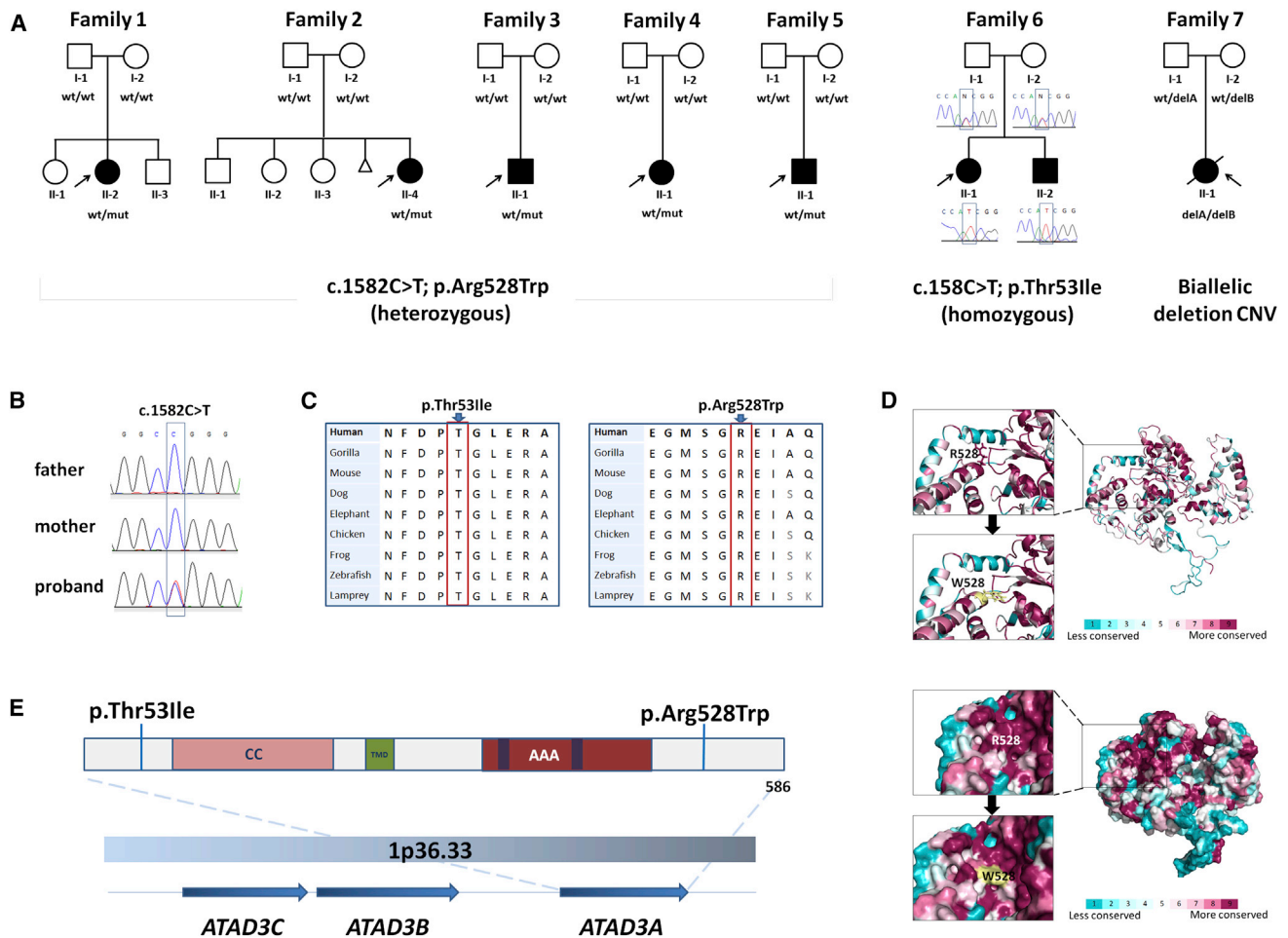
Figure 1. Pedigrees and *ATAD3A* Variant Details
(A) Pedigrees of studied families, indicating the recurrent de novo single-nucleotide variant (SNV) in *ATAD3A* in families 1–5, a homozygous SNV in family 6, and compound heterozygous deletion copy-number variants (CNVs) in family 7.
(B) Sanger validation of the *ATAD3A* variant in family 1.
(C) The p.Thr53Ile and p.Arg528Trp substitutions alter conserved residues.
(D) Protein structure prediction shows replacement of the arginine long side chain by a flat aromatic ring of tryptophan. Color spectrum indicates high conservation of the Arg528 residue. Surface structure modeling indicates that the arginine at position 528 resides in a conserved pocket, possibly a functional site. The mutation alters the configuration of the pocket.
(E) Schematic representation of ATAD3A (isoform 2) with indication of the coiled-coil domain (CC), transmembrane domain (TMD), and AAA domain including Walker A and Walker B ATP-binding and ATPase domains, respectively. Localization of the altered residues in families 1–6 is indicated. The three human ATAD3 genes are located in tandem on chromosome 1p36.33.

Homozygous *ATAD3A* Single-Nucleotide Variant Identified in Siblings with Congenital Cataract, Ataxia, and Seizures

In a sixth family (Figures 1A and 2I–2L), two siblings born to distantly related parents presented with motor developmental delay, speech delay, congenital cataracts, seizures, ataxia, hypotonia, and reduced muscle strength in the extremities (Tables 1, S1, Supplemental Data). Magnetic resonance imaging (MRI) revealed hypoplasia of the optic nerves and cerebellar atrophy (Figures 2O and S6), and magnetic resonance spectroscopy (MRS) revealed a moderate reduction of N-acetyl aspartate to creatine (NAA/Cr) ratio in the cerebellum, indicating neuronal-axonal degeneration. No CSF lactate was detected. Muscle biopsy of the male sibling showed slight increase of Oil Red O (ORO) and sub-sarcolemmal COX activities. Mitochondrial respira-tory chain enzyme analysis in muscle homogenate and in skin fibroblasts revealed normal activities (Table S4). The variant with the strongest bioinformatic predictions shared by the siblings was a homozygous *ATAD3A* variant (g.chr1:1447806C>T [hg19]; GenBank: NM_001170535.1; c.158C>T [p.Thr53Ile]), found in an ~700 kb run of homozygosity (ROH). Bioinformatic predictions and in silico modeling supported pathogenicity (Table S3, Figure S7). The genetic data suggest that biallelic variation in *ATAD3A* might lead to a distinct neurological phenotype as a recessive disease trait.

Biallelic Deletion of *ATAD3A* Is Associated with Infantile Lethality

The high homology between the three *ATAD3* paralogs, as depicted by Miropeats alignment of this region to itself
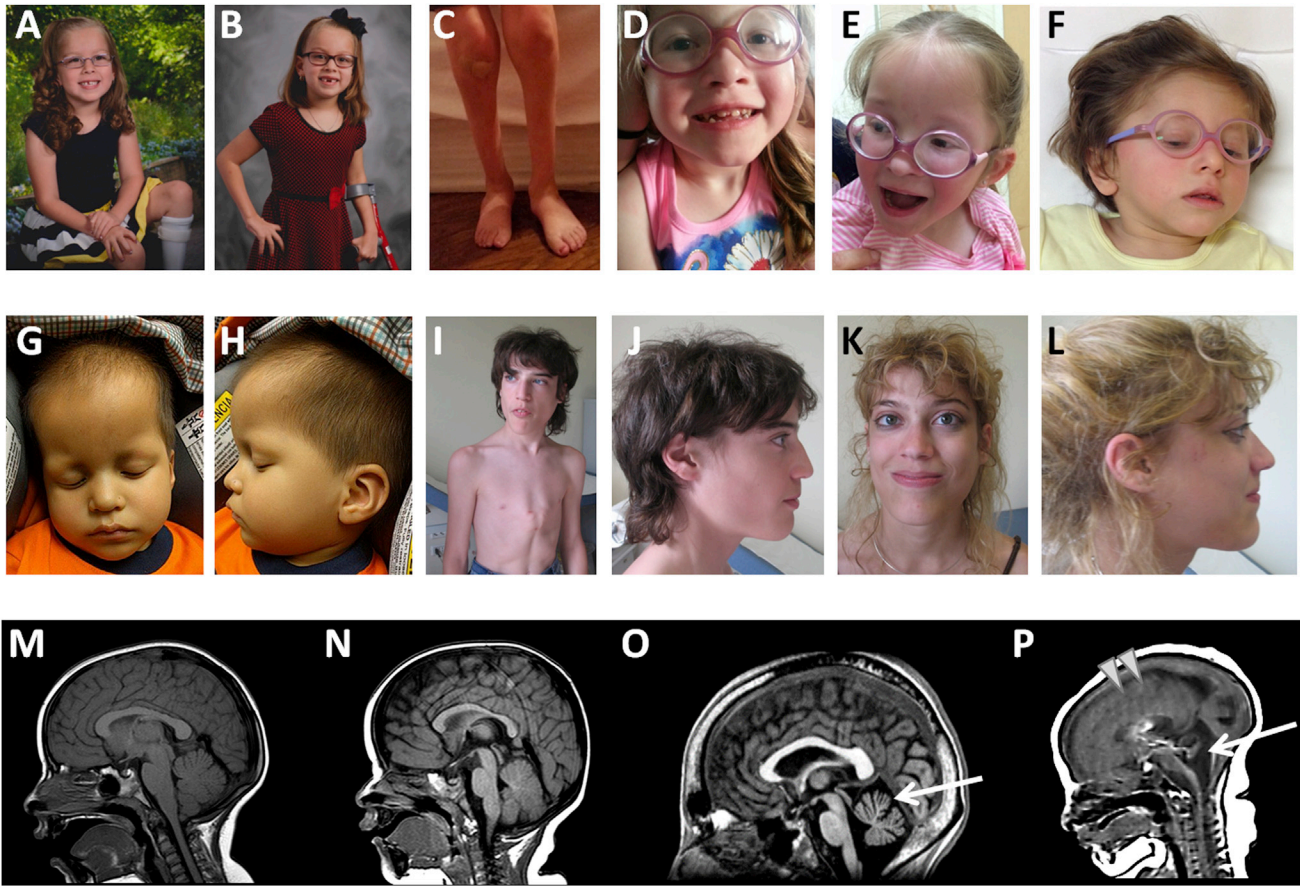
Figure 2. Clinical Findings of Affected Individuals
(A–C) Family 1, II-2 at 6 years (A) and 8 years (B), showing high forehead (B) and marked atrophy of the lower legs (C).
(D and E) Family 2, II-4 at 5 years with high forehead, small nose, and thin hair.
(F) Family 4, II-1 at 5 years with triangular facies, micrognathia, and low-set ears.
(G and H) Family 5, II-1 at 23 months, with frontal bossing, deep set eyes, and micrognathia.
(I–L) Individuals II-2 (I, J) and II-1 (K, L) from family 6, demonstrating elongated face, triangular nose and prognathism, and pectus carinatum (I).
(M–P) Mid-sagittal T1-weighted brain magnetic resonance imaging (MRI) images from affected individuals.
(M and N) Individuals with heterozygous recurrent de novo variant show either no significant abnormalities (M, family 1, II-2 at 6 years) or prominent extra-axial spaces and incomplete myelination (N, family 5, II-1 at 8 months).
(O) Family 6, II-1, harboring a homozygous *ATAD3A* missense variant, had moderate atrophy of the cerebellum (arrow) at age 26 years.
(P) MRI of family 7, II-1, with biallelic deletion of *ATAD3A*, showed very poor gyration and sulcation (arrowheads) and hypoplastic cerebellum, vermis, and brainstem (arrow).

(Figure 3A), provides an endogenous genome architecture as substrate for nonallelic homologous recombination (NAHR) in this region and is predicted to make this locus susceptible to genomic instability.[49,50] Indeed, multiple heterozygous CNVs at the *ATAD3* locus have been reported in the Database of Genomic Variants (DGV, Figure S8A), yet no biallelic CNVs are reported.

Through analysis of WES data read depth, we identified a case subject with a biallelic deletion involving exons 1–5 of *ATAD3A* (Figure 3B). The proband (BAB8780 or family 7, II-1 in Figure 1A) had reduced fetal movement, respiratory failure requiring intubation at birth, cloudy corneas, seizures, and cerebellar and brainstem hypoplasia (Figure 2P). He died at 13 days. Targeted array comparative genomic hybridization (aCGH) (Figures S9A and S9B) and droplet digital PCR on parental samples (Figure 3C), followed by ampli-

fication of the breakpoint junctions (Figures 3D and 3E), revealed two distinct deletions. In the maternal sample (BAB8733), deletion of a ~38 kb segment was mediated by NAHR between the highly homologous fifth introns of *ATAD3B* and *ATAD3A* (Figure 4A). The approximate breakpoint junctions are located within chr1: 1,416,438–1,417,192 and 1,454,542–1,455,296 (hg19). Sanger sequencing showed a stretch of 754 bp with 100% identity at the breakpoint junctions, including an *Alu*Sx1 element (Figures S8B and S10A). In the paternal sample (BAB8734), deletion of a ~68 kb segment was mediated by NAHR between the highly homologous region spanning exons 7 and 11 in *ATAD3C* and *ATAD3A*, respectively (Figure 4). The approximate breakpoint junctions are located within chr1: 1,391,287–1,392,247 and chr1: 1,459,379–1,460,339 (hg19). Sanger sequencing revealed a stretch of
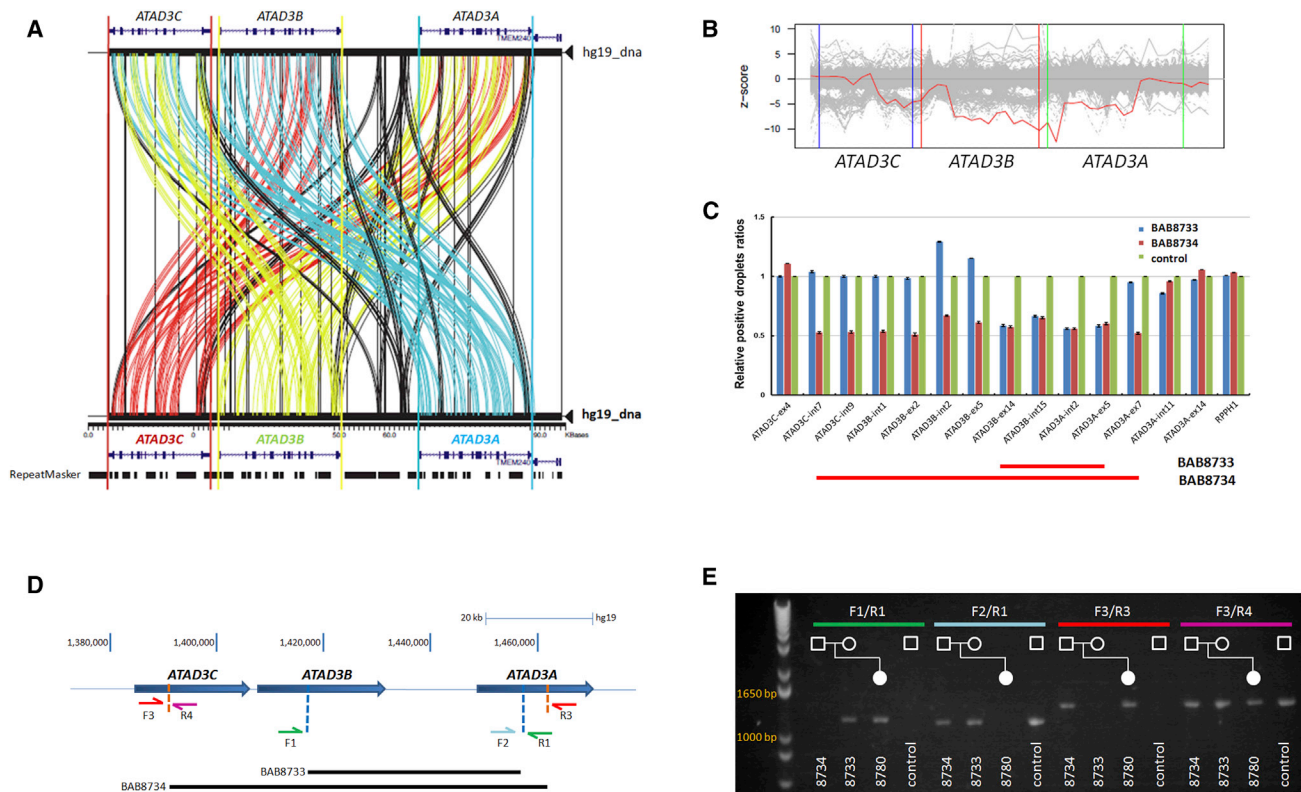
Figure 3. Compound Heterozygous Copy-Number Variation in Family 7

(A) Miropeats alignment of the *ATAD3* region indicates homology of the three *ATAD3* paralogs. *ATAD3C* reference sequence is indicated in red, *ATAD3B* reference sequence is indicated in green, and *ATAD3A* reference sequence is indicated in blue.

(B) Target Z score of PCA-normalized read depths for 44 exon targets of the three *ATAD3* genes. Comparative read depth data obtained from 2,634 WES samples are shown in gray (clinical collection). Family 7, II-1 is shown in red. Target Z score of PCA-normalized read depths for 16 exons (x axis) spanning portions of *ATAD3B* and *ATAD3A* have large negative Z scores (y axis), indicating a copy loss of both alleles.

(C) Droplet Digital PCR (ddPCR) detected a larger heterozygous deletion in BAB8734 (father) than the heterozygous deletion in BAB8733 (mother). Primer pairs targeting various exonic or intronic regions of *ATAD3C*, *ATAD3B*, and *ATAD3A* and a control primer pair targeting *RPPH1* were used to perform ddPCR in BAB8733 (mother), BAB8734 (father), and a control individual N/A10851. *RPPH1* is a gene known to have exactly two copies in the human genome. Ratios of concentrations of positive droplets were plotted for each amplicon tested against the control individual. For a region without deletion, the expected ratio is ~1, whereas for heterozygous deletion, the expected ratio is ~0.5 (one deleted copy-number versus two copies). Corresponding raw data of ddPCR and primer sequences are shown in Table S1.

(D) Schematic of primer design targeting maternal and paternal deletions and wild-type alleles. PCR amplicons indicating segregation of maternal deletion allele (F1/R1) and paternal deletion allele (F3/R3). Note that proband (BAB8780) lacks wild-type allele amplified by F2/R1 but does have wild-type allele amplified by F3/R4 since the latter is positioned outside the maternal deletion and can be amplified from this allele.

(E) Results of PCR breakpoint analysis. Proband inherited both the maternal and paternal deletions.

960 bp with 99.7% homology at the breakpoint junction and 273 bp with 100% identity (Figure S10B). The paternal deletion was not found in 100 population-matched white controls, as evaluated by breakpoint junction PCR (data not shown). The proband inherited both deletions (Figure 3E), presumably leading to loss of both functional copies of *ATAD3A*. A heterozygous deletion similar to that observed in the mother was identified previously in 1/15,767 individuals (dbVar: nsv545010),[51] and a heterozygous deletion similar to that of the father—spanning from *ATAD3C* to *ATAD3A*—was present in 13/873 (~1.5%) individuals (dbVAR: dgv2e212).[52] The latter frequency suggests that homozygous or compound heterozygous deletions of *ATAD3A* may be a source of morbidity in humans. This outcome may be under-recognized, perhaps due to genomic complexity at the locus, issues with the ability

to uniquely map sequencing reads to the reference sequencing reads because of the presence of the gene family at this locus, poor coverage on some clinically available aCGH platforms, and small size of these intergenic deletion CNVs.

We also identified a subject (BAB761) with an apparent homozygous deletion of *ATAD3C* and *ATAD3B*, not involving *ATAD3A* and confirmed by aCGH and ddPCR (Figures S9C, S9D, and S11). BAB761 had previously been assigned a clinical and molecular diagnosis of Smith-Magenis syndrome (SMS [MIM: 182290]), associated with a second, heterozygous deletion on chromosome 17p11.2 encompassing *RAI1* (MIM: 607642).[53] Hence, we concluded that homozygous deletion of *ATAD3C* and *ATAD3B* does not have a substantial impact on phenotype and narrowed the critical region for the *ATAD3* locus to *ATAD3A*.
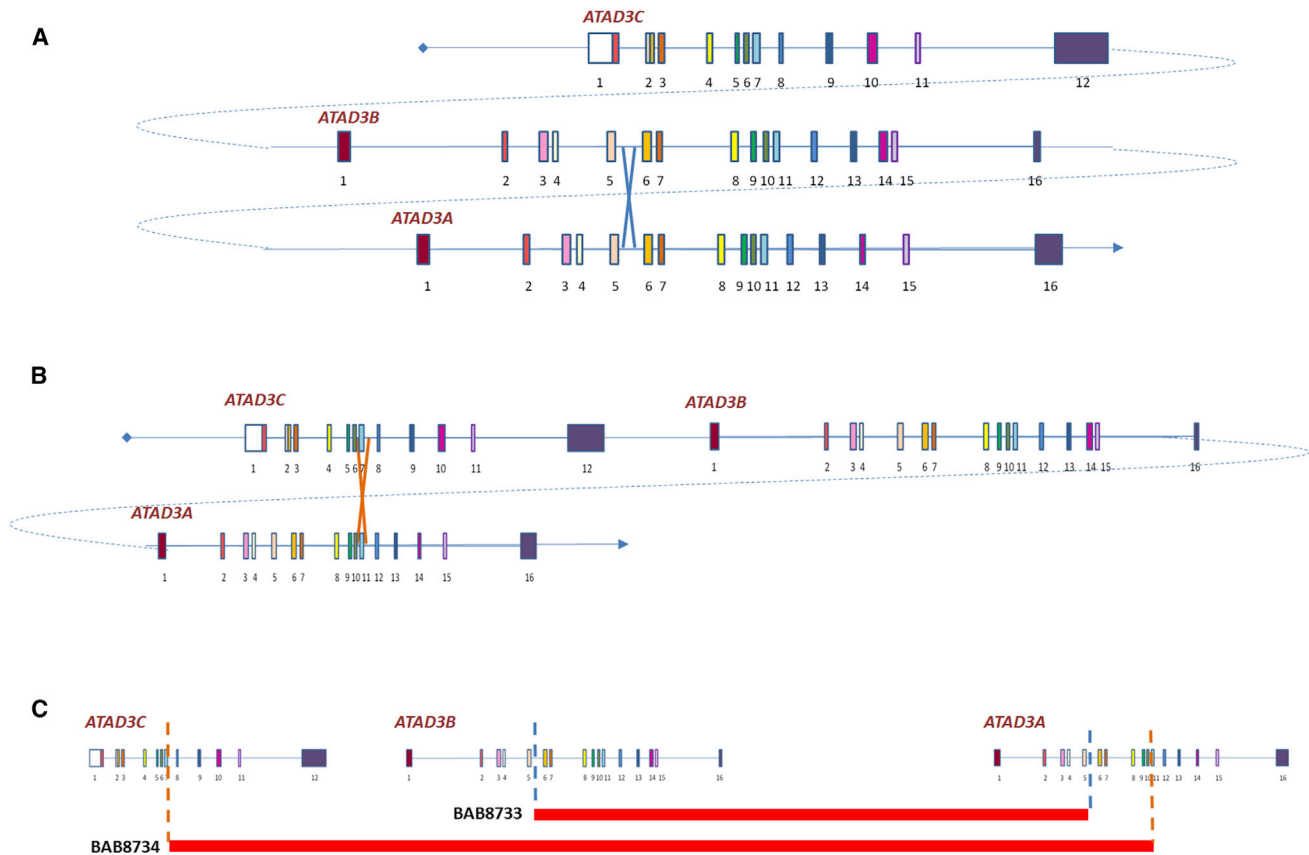
Figure 4. CNVs in Family 7 Are Mediated by NAHR
(A) Homologous exons of the three *ATAD3* genes are represented by similar colors. The deletion in BAB8733 (mother) is mediated by nonallelic homologous recombination (NAHR) between the fifth introns of *ATAD3B* and *ATAD3A*.
(B) The deletion in BAB8734 (father) is mediated by NAHR between the region of exon 7 of *ATAD3C* and exon 11 of *ATAD3A*.
(C) The boundaries of both deletions are represented by dotted lines.

The Fly p.Arg534Trp Variant Causes a Dramatic Loss of Mitochondria in Flies

To functionally evaluate the potential pathogenicity of the recurrent de novo p.Arg528Trp variant, we generated transgenic flies harboring a wild-type or variant UAS-cDNA copy (p.Arg534Trp, equivalent to human p.Arg528Trp) of *bor*, the fly homolog of *ATAD3A* (*UAS-bor^WT^* and *UAS-bor^R534W^*). This allowed us to drive these cDNA with tissue-specific Gal4 drivers. Ubiquitous expression of *bor^R534W^* (*tub-* or *Ubi-Gal4 > UAS-bor^R534W^*), as well as pan-neuronal (*n-syb-panneuronal-Gal4 > UAS-bor^R534W^*) and motor neuron-specific (*D42-motorneurons-Gal4 > UAS-bor^R534W^*) expression, all caused lethality, whereas *bor^WT^* expression (*tub-, Ubi-Gal4, n-syb-panneuronal-Gal4,* or *D42-motorneurons-Gal4 > UAS-bor^WT^*) did not affect viability or cause any other obvious phenotype (Figure 5A). Muscle-specific expression of *bor^R534W^* (*C57-muscles-Gal4 > UAS-bor^R534W^*) led to ~90% lethality (Figure 5A). Hence, *bor^R534W^* expression causes dramatic reductions in survival when expressed in all neurons, motor neurons, or muscles, suggesting that the protein is highly toxic. It may therefore act as either a dominant-negative or a gain-of-function mutation.

At the cellular level, we noted that motor neurons expressing *bor^R534W^* exhibited a dramatic reduction in mitochondria in cell bodies in the ventral nerve cord (VNC), axons, and synaptic boutons (Figures 5B–5E), suggesting that expression of the variant severely affects mitochondrial biogenesis[54] or mitochondrial dynamics, leading to mitophagy. When expressed specifically in larvae body wall muscles, the signal intensity of the mitochondrial marker ATP5A in *bor^R534W^*-expressing muscles was significantly reduced when compared to *bor^WT^*-expressing muscles or wild-type controls, consistent with our observation in motor neurons (Figures 6A and 6C). Transmission electron microscopy (TEM) revealed that muscles expressing *bor^R534W^* contain very few small mitochondria with highly aberrant cristae (Figure 6B, arrowheads) and display a substantive increase in autophagic intermediates (Figure S12). In contrast, overexpression of *bor^WT^* resulted in an increase in the number of large elongated mitochondria (Figures 6B and 6D). These data indicate that Bor^WT^ promotes fusion or inhibits fission, or affects both, whereas Bor^R534W^ inhibits fusion or promotes fission.

Fibroblasts from individual II-2 in family 1 at age 9 years showed a significant increase in mitophagy (Figures 6E, 6F, and S13) and a reduction, though not significant, in mitochondrial content (Figure S14). In conjunction with the fly data, this indicates that the p.Arg528Trp variant interferes
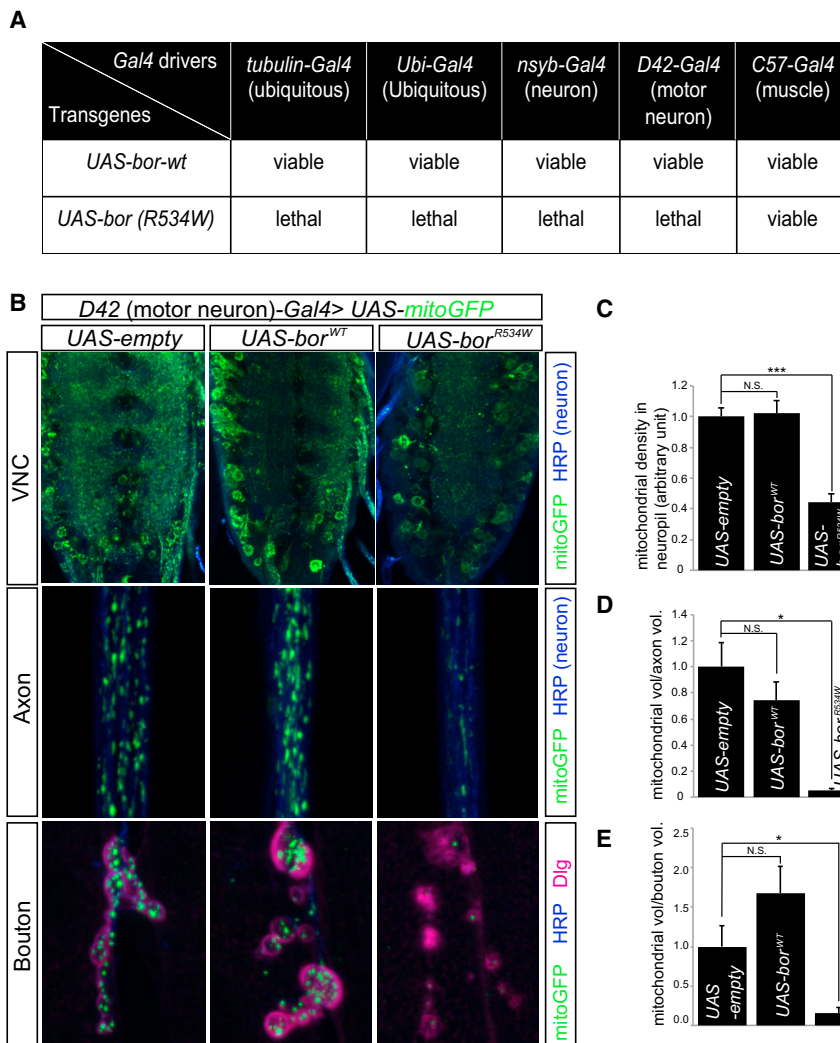
Figure 5. Expression of *Drosophila* ATAD3A Ortholog *bor* with p.Arg534Trp Leads to a Decrease in Mitochondria in Motor Neurons

(A) Effects of expression of wild-type *bor* and *bor*[R534W], driven by different *Gal4* drivers, on viability.

(B) Confocal micrographs of ventral nerve cord (VNC), axons, and boutons from third instar larvae carrying *D42-Gal4* and *UAS-mito-GFP* (green) together with *UAS-empty* (control), *UAS-bor*[WT], or *UAS-bor*[R534W]. Neurons are labeled by HRP (blue) and boutons by Dlg (red).

(C) Quantification of mitochondrial density in VNC neuropil in control, *UAS-bor*[WT], or *UAS-bor*[R534W] larvae carrying *D42-Gal4*, *UAS-mito-GFP* together with the respective vectors.

(D and E) Quantification of mitochondrial volume in axons (D) and in boutons (E) of larvae carrying *D42-Gal4*, *UAS-mito-GFP* together with *UAS-empty*, *UAS-bor*[WT], or *UAS-bor*[R534W].

(C–E) Error bars indicate standard error of the mean (SEM). p values were calculated by Student's t test. $*p < 0.05$, $***p < 0.001$. N.S. indicates not statistically significant.

associated with the recurrent de novo c.1582C>G variant, observed in five families, manifests within a phenotypic and metabolic spectrum including global developmental delay, hypotonia, optic atrophy, axonal neuropathy, hypertrophic cardiomyopathy, lactic acidosis, and/or increased excretion of Krebs cycle intermediates. Several of these features overlap with phenotypes associated with other mitochondrial fission and fusion proteins (Figure S5), as exemplified by *DNM1L* (severe developmental delay, optic atrophy, peripheral neuropathy, lactic acidemia [MIM: 614388]),[10,11] *MFN2* (axonal peripheral neuropathy and variable optic atrophy [MIM: 609260]),[5,7] *OPA1* (optic atrophy, variable peripheral neuropathy,[8] and recently described hypertrophic cardiomyopathy [MIM: 165500 and 125250]),[9] and *SLC25A46* (axonal peripheral neuropathy and optic atrophy [MIM: 616505]).[13]

The recurrence of the de novo c.1582C>T variant in five distinct probands is likely attributable to a mutational hotspot at a CpG dinucleotide.[41–43] However, it is unclear from this initial study whether this is the only variant that can lead to a dominant phenotype, or if the bias is due to the CpG mutational hotspot. Three of the most highly mutable nucleotides known in the human genome are at CpG sites (*FGFR3* [MIM: 100800], *DMD* [MIM: 310200], and *FGFR2* [MIM: 101200]),[55] with two more recent examples (*KCNC1* [MIM: 616187][56] and *PACS1* [MIM: 607492]).[57]

with mitochondrial dynamics by either promoting fission or inhibiting fusion, which in turn may trigger mitophagy.

To assess the loss-of-function phenotypes associated with *bor*, we performed TEM on first instar larvae that lack *bor* just prior to their death and identified a dramatic decrease in mitochondrial content, similar to overexpression of Bor[R534W] (Figures 6G and 6H). Given the similarities between the phenotypes associated with the loss of function of *bor* and the overexpression of *bor*[R534W], we propose that Bor[R534W] acts as a strong dominant-negative mutation. This is supported by our finding that steady-state levels of ATAD3A protein in fibroblasts of the proband in family 4 are comparable to controls, when assayed both in total lysate and in crude mitochondria (Figure S15).

Discussion

We report eight individuals from seven families with monoallelic or biallelic variation involving both SNVs and CNVs at the *ATAD3A* locus, all presenting with a primarily neurologic disease. The clinical syndrome
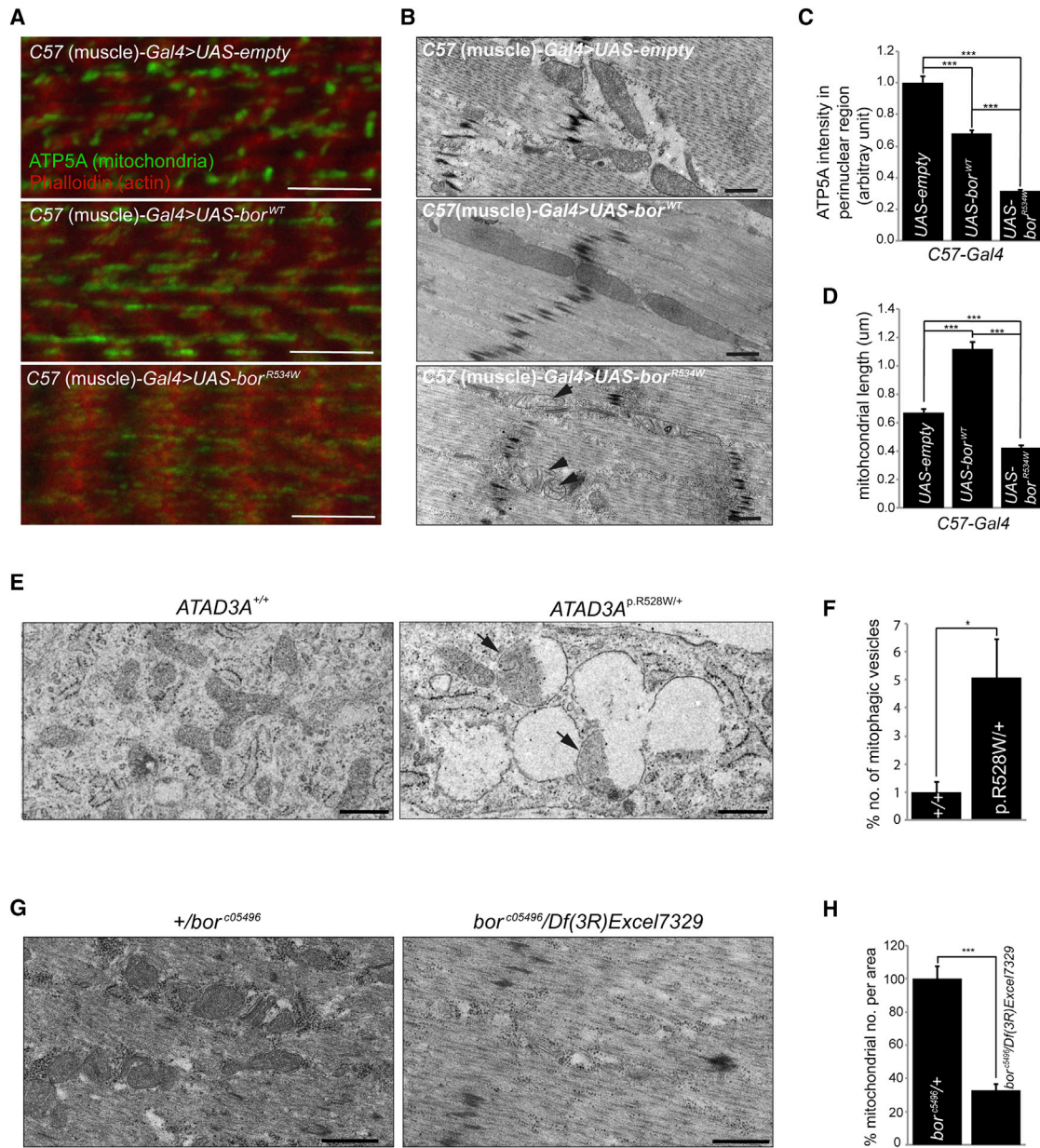
Figure 6. Expression of *Drosophila* ATAD3 Ortholog *bor* with p.Arg534Trp Variant in Muscle Causes a Decrease of Mitochondria

(A) Confocal micrographs of muscle from third instar larvae carrying *C57-Gal4* together with *UAS-empty* (control), *UAS-bor^WT^*, or *UAS-bor^R534W^*. ATP5A (green) labels mitochondria. Phalloidin (red) labels actin. Scale bars represent 10 μm.

(B) TEM of muscle from third instar larvae carrying *C57-Gal4* together with *UAS-empty* (control), *UAS-bor^WT^*, or *UAS-bor^R534W^*. Scale bars represent 500 nm.

(C) Quantification of ATP5A signal intensity in muscle of larvae carrying *C57-Gal4*, together with *UAS-empty*, *UAS-bor^WT^*, or *UAS-bor^R534W^* from confocal images (A).

(D) Quantification of mitochondrial length in muscle of larvae carrying *C57-Gal4*, together with *UAS-empty*, *UAS-bor^WT^*, or *UAS-bor^R534W^* from TEM images (B).

(E) TEM of fibroblasts from an affected individual (BAB8644, *ATAD3A^p.R528W/+^*) and control (*ATAD3A^+/+^*) fibroblasts. Scale bars represent 500 nm.

(F) Quantification of mitophagic vesicles (E, arrows) among all vesicles in affected (BAB8644, *ATAD3A^R528W/+^*) and control (*ATAD3A^+/+^*) fibroblasts.

(G) TEM of muscle from first instar larvae for *bor* mutants (*bor^c05496^/Df (3R)Excel7329*) and control (*bor^c05496^/+*). Scale bars represent 500 nm.

(H) Quantification of mitochondria per area in *bor* mutants (*bor^c05496^/Df (3R)Excel7329*) and control (*bor^c05496^/+*).

(C, D, F, H) Error bars indicate SEM. p values were calculated by Student's t test. *p < 0.05. ***p < 0.001. N.S. indicates not statistically significant.

The features associated with the biallelic SNV identified in two siblings include ataxia, epilepsy, and congenital cataracts, while the compound heterozygous CNVs conferred a more severe phenotype of respiratory insufficiency at birth, cloudy corneas, hypoplastic cerebellum and brainstem, and seizures. Monoallelic and biallelic pathogenic variation at a single locus has been observed for numerous genes, including mitochondrial genes (e.g., OPA1 [MIM: 605290], SLC25A4 [MIM: 103220], AARS [MIM: 601065], EMC1 [MIM: 616846], MAB21L2 [MIM: 604357], and NALCN [MIM: 611549]).[9,58–63] There is often a difference in severity of phenotype between the monoallelic and biallelic forms of disease, although in many cases, the same organ systems are involved. In the case of ATAD3A, there is primarily involvement of the nervous system and the eye in both monoallelic and biallelic forms.

The ExAC constraint metric for loss of function is 0.04, indicating a high tolerance for heterozygous loss-of-function alleles. Indeed, individuals harboring a heterozygous deletion involving the ATAD3 genes (i.e., parents in family 7) are unaffected. These data suggest a dominant-negative pathogenic mechanism or a gain-of-function mechanism for the recurrent de novo variant rather than haploinsufficiency. The data from Drosophila show that overexpression of a wild-type cDNA, one form of a gain-of-function experiment, does not affect viability and leads to an expansion of mitochondrial size. However, expression of the de novo variant in many tissues in flies is toxic and leads to death. The observed phenotype in these tissues phenocopies the null mutant and yields effects opposite to those seen with overexpression of the wild-type cDNA. Hence, experimental evidence indicates that ATAD3A p.Arg528Trp behaves as a dominant-negative, or antimorphic, allele. This conclusion is supported further by the proposed oligomeric formation of ATAD3 proteins.[15]

Although most species have only one ATAD3 gene locus, primates have three ATAD3 paralogs (ATAD3A, ATAD3B, ATAD3C), which appear to have evolved by duplication of a single precursor gene. In humans, the three genes are located in tandem on chromosome 1p36.33 (Figure 1E). Multiple isoforms of the three ATAD3 genes are generated by transcriptional and post-transcriptional events. The major ATAD3A isoform, p66, is ubiquitously expressed, whereas the major ATAD3B isoform, p67, was specifically detected in embryo muscle, placenta, and adult brain and heart. ATAD3C is missing four exons as compared to ATAD3A, suggesting that it may be a pseudogene. In the mouse, a single Atad3 gene is located on murine chromosome 4 and encodes a major ubiquitous isoform and several smaller tissue- and/or temporal-specific isoforms.[23] ATAD3 function is essential in the mouse for early post-implantation development. ATAD3-deficient embryos die around E7.5 due to growth retardation and a defective development of the trophoblast lineage; heterozygotes seem unaffected.[22] Given the severe phenotype and respiratory insufficiency of family 7, II-1, it may be surmised that biallelic deletions involving ATAD3A will lead to fetal demise. The potential salvage of lethality in this individual during development by a theoretical fusion protein extending from ATAD3B to ATAD3A and under control of the ATAD3B promoter, active during embryonic development,[23,64] warrants further investigation. Moreover, the potential embryonic lethality of the homozygous ~68 kb ATAD3C-ATAD3A allele could distort Mendelian expectations despite the observed relatively high (~1.5%) carrier frequency in the white population.

ATAD3A has two coiled-coil domains with high oligomerization probability within the N terminus, followed by a predicted transmembrane segment in the central part of the molecule and a conserved ATPase domain in the C terminus (Figure 1E).[15,23] Oligomerization of ATAD3A monomers is further supported by findings showing that other AAA proteins assemble as hexameric rings.[65] Studies in human U373 cells demonstrated that defective ATP-binding ATAD3A mutants interfere with normal oligomer functions and lead to fragmentation of mitochondria.[15] In the current study, we observed a dramatic loss of mitochondria in motor neurons of transgenic mutant flies (Figures 5B–5E), highly aberrant mitochondrial morphology, and an increase in autophagic intermediates in the fly muscle (Figure S12). Moreover, overexpression of wild-type bor resulted in an increased number of large elongated mitochondria (Figures 6B and 6D) whereas TEM of homozygous null flies showed a dramatic decrease in size and number of mitochondria (Figures 6G and 6H). Finally, fibroblasts from an affected individual harboring the p.Arg528Trp variant showed a significant increase in mitophagy (Figures 6E, 6F, and S13) and a reduction, though not statistically significant, in mitochondrial content (Figure S14). The aggregate data suggest that the production of small aberrant mitochondria probably results in increased mitophagy and a significant reduction of mitochondrial content. The molecular mechanisms remain to be elucidated.

In summary, we have identified monoallelic and biallelic variation involving both SNVs and CNVs at the ATAD3A locus. We propose that the dominant p.Arg528Trp variant disturbs ATAD3A function by a dominant-negative mechanism, while the recessive CNVs lead to infantile lethality through loss of ATAD3A function. These data suggest an allelic series with decreasing severity: c.1582C>T (p.Arg528Trp) (antimorph) > ATAD3A deletion CNV (null) > c.158C>T (p.Thr53Ile) (hypomorph). The previously described function of ATAD3A in mitochondrial dynamics and its co-immunoprecipitation with MFN2 and OPA1, in conjunction with the phenotypic and functional data presented herein, indicates that ATAD3A is essential in humans.

Accession Numbers

Supplemental Data

Supplemental Data include detailed clinical case reports, 15 figures, and 4 tables and can be found with this article online at http://dx.doi.org/10.1016/j.ajhg.2016.08.007.

Web Resources

1000 Genomes, http://www.1000genomes.org
Atherosclerosis Risk in Communities Study (ARIC), http://drupal.cscc.unc.edu/aric/
Baylor Genetics, http://www.bmgl.com
CADD, http://cadd.gs.washington.edu/
ConSurf, consurf.tau.ac.il
Database of Genomic Variants (DGV), http://dgv.tcag.ca/dgv/app/home
Ensembl Genome Browser, http://www.ensembl.org/index.html
ExAC Browser, http://exac.broadinstitute.org/
GeneMatcher, https://genematcher.org/
HMZDelFinder, https://github.com/BCM-Lupskilab/HMZDelFinder
NHLBI Exome Sequencing Project (ESP) Exome Variant Server, http://evs.gs.washington.edu/EVS/
OMIM, http://www.omim.org/
PyMOL, http://www.pymol.org
R statistical software, http://www.r-project.org/
SIFT, http://sift.bii.a-star.edu.sg/

References

1. Mishra, P., and Chan, D.C. (2014). Mitochondrial dynamics and inheritance during cell division, development and disease. Nat. Rev. Mol. Cell Biol. *15*, 634–646.
2. Niemann, A., Ruegg, M., La Padula, V., Schenone, A., and Suter, U. (2005). Ganglioside-induced differentiation associated protein 1 is a regulator of the mitochondrial network: new implications for Charcot-Marie-Tooth disease. J. Cell Biol. *170*, 1067–1078.
3. Pareyson, D., Saveri, P., Sagnelli, A., and Piscosquito, G. (2015). Mitochondrial dynamics and inherited peripheral nerve diseases. Neurosci. Lett. *596*, 66–77.
4. Züchner, S., Mersiyanova, I.V., Muglia, M., Bissar-Tadmouri, N., Rochelle, J., Dadali, E.L., Zappia, M., Nelis, E., Patitucci, A., Senderek, J., et al. (2004). Mutations in the mitochondrial GTPase mitofusin 2 cause Charcot-Marie-Tooth neuropathy type 2A. Nat. Genet. *36*, 449–451.
5. Züchner, S., De Jonghe, P., Jordanova, A., Claeys, K.G., Guergueltcheva, V., Cherninkova, S., Hamilton, S.R., Van Stavern, G., Krajewski, K.M., Stajich, J., et al. (2006). Axonal neuropathy with optic atrophy is caused by mutations in mitofusin 2. Ann. Neurol. *59*, 276–281.
6. Verhoeven, K., Claeys, K.G., Züchner, S., Schröder, J.M., Weis, J., Ceuterick, C., Jordanova, A., Nelis, E., De Vriendt, E., Van Hul, M., et al. (2006). *MFN2* mutation distribution and genotype/phenotype correlation in Charcot-Marie-Tooth type 2. Brain *129*, 2093–2102.
7. Rouzier, C., Bannwarth, S., Chaussenot, A., Chevrollier, A., Verschueren, A., Bonello-Palot, N., Fragaki, K., Cano, A., Pouget, J., Pellissier, J.F., et al. (2012). The *MFN2* gene is responsible for mitochondrial DNA instability and optic atrophy 'plus' phenotype. Brain *135*, 23–34.
8. Yu-Wai-Man, P., Griffiths, P.G., Gorman, G.S., Lourenco, C.M., Wright, A.F., Auer-Grumbach, M., Toscano, A., Musumeci, O., Valentino, M.L., Caporali, L., et al. (2010). Multi-system neurological disease is common in patients with *OPA1* mutations. Brain *133*, 771–786.
9. Spiegel, R., Saada, A., Flannery, P.J., Burté, F., Soiferman, D., Khayat, M., Eisner, V., Vladovski, E., Taylor, R.W., Bindoff, L.A., et al. (2016). Fatal infantile mitochondrial encephalomyopathy, hypertrophic cardiomyopathy and optic atrophy associated with a homozygous *OPA1* mutation. J. Med. Genet. *53*, 127–131.
10. Chao, Y.H., Robak, L.A., Xia, F., Koenig, M.K., Adesina, A., Bacino, C.A., Scaglia, F., Bellen, H.J., and Wangler, M.F. (2016). Missense variants in the middle domain of DNM1L in cases of infantile encephalopathy alter peroxisomes and mitochondria when assayed in *Drosophila*. Hum. Mol. Genet. *25*, 1846–1856.
11. Waterham, H.R., Koster, J., van Roermund, C.W., Mooyer, P.A., Wanders, R.J., and Leonard, J.V. (2007). A lethal defect of mitochondrial and peroxisomal fission. N. Engl. J. Med. *356*, 1736–1741.
12. Shahni, R., Cale, C.M., Anderson, G., Osellame, L.D., Hambleton, S., Jacques, T.S., Wedatilake, Y., Taanman, J.W., Chan, E., Qasim, W., et al. (2015). Signal transducer and activator of transcription 2 deficiency is a novel disorder of mitochondrial fission. Brain *138*, 2834–2846.

13. Abrams, A.J., Hufnagel, R.B., Rebelo, A., Zanna, C., Patel, N., Gonzalez, M.A., Campeanu, I.J., Griffin, L.B., Groenewald, S., Strickland, A.V., et al. (2015). Mutations in *SLC25A46*, encoding a UGO1-like protein, cause an optic atrophy spectrum disorder. Nat. Genet. *47*, 926–932.

14. Niemann, A., Wagner, K.M., Ruegg, M., and Suter, U. (2009). *GDAP1* mutations differ in their effects on mitochondrial dynamics and apoptosis depending on the mode of inheritance. Neurobiol. Dis. *36*, 509–520.

15. Gilquin, B., Taillebourg, E., Cherradi, N., Hubstenberger, A., Gay, O., Merle, N., Assard, N., Fauvarque, M.O., Tomohiro, S., Kuge, O., and Baudier, J. (2010). The AAA+ ATPase ATAD3A controls mitochondrial dynamics at the interface of the inner and outer membranes. Mol. Cell. Biol. *30*, 1984–1996.

16. He, J., Cooper, H.M., Reyes, A., Di Re, M., Sembongi, H., Litwin, T.R., Gao, J., Neuman, K.C., Fearnley, I.M., Spinazzola, A., et al. (2012). Mitochondrial nucleoid interacting proteins support mitochondrial protein synthesis. Nucleic Acids Res. *40*, 6109–6121.

17. Issop, L., Fan, J., Lee, S., Rone, M.B., Basu, K., Mui, J., and Papadopoulos, V. (2015). Mitochondria-associated membrane formation in hormone-stimulated Leydig cell steroidogenesis: role of ATAD3. Endocrinology *156*, 334–345.

18. Rone, M.B., Midzak, A.S., Issop, L., Rammouz, G., Jagannathan, S., Fan, J., Ye, X., Blonder, J., Veenstra, T., and Papadopoulos, V. (2012). Identification of a dynamic mitochondrial protein complex driving cholesterol import, trafficking, and metabolism to steroid hormones. Mol. Endocrinol. *26*, 1868–1882.

19. Teng, Y., Ren, X., Li, H., Shull, A., Kim, J., and Cowell, J.K. (2016). Mitochondrial ATAD3A combines with GRP78 to regulate the WASF3 metastasis-promoting protein. Oncogene *35*, 333–343.

20. You, W.C., Chiou, S.H., Huang, C.Y., Chiang, S.F., Yang, C.L., Sudhakar, J.N., Lin, T.Y., Chiang, I.P., Shen, C.C., Cheng, W.Y., et al. (2013). Mitochondrial protein ATPase family, AAA domain containing 3A correlates with radioresistance in glioblastoma. Neuro-oncol. *15*, 1342–1352.

21. Fang, H.Y., Chang, C.L., Hsu, S.H., Huang, C.Y., Chiang, S.F., Chiou, S.H., Huang, C.H., Hsiao, Y.T., Lin, T.Y., Chiang, I.P., et al. (2010). ATPase family AAA domain-containing 3A is a novel anti-apoptotic factor in lung adenocarcinoma cells. J. Cell Sci. *123*, 1171–1180.

22. Goller, T., Seibold, U.K., Kremmer, E., Voos, W., and Kolanus, W. (2013). Atad3 function is essential for early post-implantation development in the mouse. PLoS ONE *8*, e54799.

23. Li, S., Lamarche, F., Charton, R., Delphin, C., Gires, O., Hubstenberger, A., Schlattner, U., and Rousseau, D. (2014). Expression analysis of *ATAD3* isoforms in rodent and human cell lines and tissues. Gene *535*, 60–69.

24. Hoffmann, M., Bellance, N., Rossignol, R., Koopman, W.J., Willems, P.H., Mayatepek, E., Bossinger, O., and Distelmaier, F. (2009). *C. elegans ATAD-3* is essential for mitochondrial activity and development. PLoS ONE *4*, e7644.

25. Yang, Y., Muzny, D.M., Xia, F., Niu, Z., Person, R., Ding, Y., Ward, P., Braxton, A., Wang, M., Buhay, C., et al. (2014). Molecular findings among patients referred for clinical whole-exome sequencing. JAMA *312*, 1870–1879.

26. Reid, J.G., Carroll, A., Veeraraghavan, N., Dahdouli, M., Sundquist, A., English, A., Bainbridge, M., White, S., Salerno, W., Buhay, C., et al. (2014). Launching genomics into the cloud: deployment of Mercury, a next generation sequence analysis pipeline. BMC Bioinformatics *15*, 30.

27. Challis, D., Yu, J., Evani, U.S., Jackson, A.R., Paithankar, S., Coarfa, C., Milosavljevic, A., Gibbs, R.A., and Yu, F. (2012). An integrative variant analysis suite for whole exome next-generation sequencing data. BMC Bioinformatics *13*, 8.

28. Li, H., Handsaker, B., Wysoker, A., Fennell, T., Ruan, J., Homer, N., Marth, G., Abecasis, G., and Durbin, R.; 1000 Genome Project Data Processing Subgroup (2009). The Sequence Alignment/Map format and SAMtools. Bioinformatics *25*, 2078–2079.

29. Wang, K., Li, M., and Hakonarson, H. (2010). ANNOVAR: functional annotation of genetic variants from high-throughput sequencing data. Nucleic Acids Res. *38*, e164.

30. Sobreira, N., Schiettecatte, F., Valle, D., and Hamosh, A. (2015). GeneMatcher: a matching tool for connecting investigators with an interest in the same gene. Hum. Mutat. *36*, 928–930.

31. Yang, J., Yan, R., Roy, A., Xu, D., Poisson, J., and Zhang, Y. (2015). The I-TASSER Suite: protein structure and function prediction. Nat. Methods *12*, 7–8.

32. Zhang, Y. (2008). I-TASSER server for protein 3D structure prediction. BMC Bioinformatics *9*, 40.

33. Ashkenazy, H., Erez, E., Martz, E., Pupko, T., and Ben-Tal, N. (2010). ConSurf 2010: calculating evolutionary conservation in sequence and structure of proteins and nucleic acids. Nucleic Acids Res. *38*, W529-33.

34. Bugiani, M., Invernizzi, F., Alberio, S., Briem, E., Lamantea, E., Carrara, F., Moroni, I., Farina, L., Spada, M., Donati, M.A., et al. (2004). Clinical and molecular findings in children with complex I deficiency. Biochim. Biophys. Acta *1659*, 136–147.

35. Fromer, M., Moran, J.L., Chambert, K., Banks, E., Bergen, S.E., Ruderfer, D.M., Handsaker, R.E., McCarroll, S.A., O'Donovan, M.C., Owen, M.J., et al. (2012). Discovery and statistical genotyping of copy-number variation from whole-exome sequencing depth. Am. J. Hum. Genet. *91*, 597–607.

36. Parsons, J.D. (1995). Miropeats: graphical DNA sequence comparisons. Comput. Appl. Biosci. *11*, 615–619.

37. Parks, A.L., Cook, K.R., Belvin, M., Dompe, N.A., Fawcett, R., Huppert, K., Tan, L.R., Winter, C.G., Bogart, K.P., Deal, J.E., et al. (2004). Systematic generation of high-resolution deletion coverage of the *Drosophila melanogaster* genome. Nat. Genet. *36*, 288–292.

38. Bischof, J., Maeda, R.K., Hediger, M., Karch, F., and Basler, K. (2007). An optimized transgenesis system for *Drosophila* using germ-line-specific phiC31 integrases. Proc. Natl. Acad. Sci. USA *104*, 3312–3317.

39. Venken, K.J., He, Y., Hoskins, R.A., and Bellen, H.J. (2006). P[acman]: a BAC transgenic platform for targeted insertion of large DNA fragments in *D. melanogaster*. Science *314*, 1747–1751.

40. Bellen, H., and Budnik, V. (2000). The Neuromuscular Junction (New York: Cold Spring Harbor Laboratory Press).

41. Cooper, D.N., Mort, M., Stenson, P.D., Ball, E.V., and Chuzhanova, N.A. (2010). Methylation-mediated deamination of 5-methylcytosine appears to give rise to mutations causing human inherited disease in CpNpG trinucleotides, as well as in CpG dinucleotides. Hum. Genomics *4*, 406–410.

42. Cooper, D.N., and Krawczak, M. (1989). Cytosine methylation and the fate of CpG dinucleotides in vertebrate genomes. Hum. Genet. *83*, 181–188.

43. Coulondre, C., Miller, J.H., Farabaugh, P.J., and Gilbert, W. (1978). Molecular basis of base substitution hotspots in *Escherichia coli*. Nature *274*, 775–780.

44. Posey, J.E., Rosenfeld, J.A., James, R.A., Bainbridge, M., Niu, Z., Wang, X., Dhar, S., Wiszniewski, W., Akdemir, Z.H., Gambin, T., et al. (2016). Molecular diagnostic experience of whole-exome sequencing in adult patients. Genet. Med. *18*, 678–685.

45. Farwell, K.D., Shahmirzadi, L., El-Khechen, D., Powis, Z., Chao, E.C., Tippin Davis, B., Baxter, R.M., Zeng, W., Mroske, C., Parra, M.C., et al. (2015). Enhanced utility of family-centered diagnostic exome sequencing with inheritance model-based analysis: results from 500 unselected families with undiagnosed genetic conditions. Genet. Med. *17*, 578–586.

46. Yang, Y., Muzny, D.M., Reid, J.G., Bainbridge, M.N., Willis, A., Ward, P.A., Braxton, A., Beuten, J., Xia, F., Niu, Z., et al. (2013). Clinical whole-exome sequencing for the diagnosis of mendelian disorders. N. Engl. J. Med. *369*, 1502–1511.

47. Campbell, I.M., Shaw, C.A., Stankiewicz, P., and Lupski, J.R. (2015). Somatic mosaicism: implications for disease and transmission genetics. Trends Genet. *31*, 382–392.

48. Campbell, I.M., Stewart, J.R., James, R.A., Lupski, J.R., Stankiewicz, P., Olofsson, P., and Shaw, C.A. (2014). Parent of origin, mosaicism, and recurrence risk: probabilistic modeling explains the broken symmetry of transmission genetics. Am. J. Hum. Genet. *95*, 345–359.

49. Carvalho, C.M., and Lupski, J.R. (2016). Mechanisms underlying structural variant formation in genomic disorders. Nat. Rev. Genet. *17*, 224–238.

50. Dittwald, P., Gambin, T., Szafranski, P., Li, J., Amato, S., Divon, M.Y., Rodríguez Rojas, L.X., Elton, L.E., Scott, D.A., Schaaf, C.P., et al. (2013). NAHR-mediated copy-number variants in a clinical population: mechanistic insights into both genomic disorders and Mendelizing traits. Genome Res. *23*, 1395–1409.

51. Cooper, G.M., Coe, B.P., Girirajan, S., Rosenfeld, J.A., Vu, T.H., Baker, C., Williams, C., Stalker, H., Hamid, R., Hannig, V., et al. (2011). A copy number variation morbidity map of developmental delay. Nat. Genet. *43*, 838–846.

52. Uddin, M., Thiruvahindrapuram, B., Walker, S., Wang, Z., Hu, P., Lamoureux, S., Wei, J., MacDonald, J.R., Pellecchia, G., Lu, C., et al. (2015). A high-resolution copy-number variation resource for clinical and population genetics. Genet. Med. *17*, 747–752.

53. Greenberg, F., Lewis, R.A., Potocki, L., Glaze, D., Parke, J., Killian, J., Murphy, M.A., Williamson, D., Brown, F., Dutton, R., et al. (1996). Multi-disciplinary clinical study of Smith-Magenis syndrome (deletion 17p11.2). Am. J. Med. Genet. *62*, 247–254.

54. Li, S., Yao, Y., Xu, R., Pesenti, S., Cottet-Rousselle, C., Rieusset, J., Tokarska-Schlattner, M., Liao, K., Schlattner, U., and Rousseau, D. (2014). ATAD3 is a limiting factor in mitochondrial biogenesis and adipogenesis of white adipocyte-like 3T3-L1 cells. Mol. Cell. Biol. Published online April 14, 2014. http://dx.doi.org/10.1128/MCB.01170-13.

55. Buzin, C.H., Feng, J., Yan, J., Scaringe, W., Liu, Q., den Dunnen, J., Mendell, J.R., and Sommer, S.S. (2005). Mutation rates in the dystrophin gene: a hotspot of mutation at a CpG dinucleotide. Hum. Mutat. *25*, 177–188.

56. Muona, M., Berkovic, S.F., Dibbens, L.M., Oliver, K.L., Maljevic, S., Bayly, M.A., Joensuu, T., Canafoglia, L., Franceschetti, S., Michelucci, R., et al. (2015). A recurrent de novo mutation in *KCNC1* causes progressive myoclonus epilepsy. Nat. Genet. *47*, 39–46.

57. Schuurs-Hoeijmakers, J.H., Oh, E.C., Vissers, L.E., Swinkels, M.E., Gilissen, C., Willemsen, M.A., Holvoet, M., Steehouwer, M., Veltman, J.A., de Vries, B.B., et al. (2012). Recurrent de novo mutations in *PACS1* cause defective cranial-neural-crest migration and define a recognizable intellectual-disability syndrome. Am. J. Hum. Genet. *91*, 1122–1127.

58. Kaukonen, J.A., Amati, P., Suomalainen, A., Rötig, A., Piscaglia, M.-G., Salvi, F., Weissenbach, J., Fratta, G., Comi, G., Peltonen, L., and Zeviani, M. (1996). An autosomal locus predisposing to multiple deletions of mtDNA on chromosome 3p. Am. J. Hum. Genet. *58*, 763–769.

59. Palmieri, L., Alberio, S., Pisano, I., Lodi, T., Meznaric-Petrusa, M., Zidar, J., Santoro, A., Scarcia, P., Fontanesi, F., Lamantea, E., et al. (2005). Complete loss-of-function of the heart/muscle-specific adenine nucleotide translocator is associated with mitochondrial myopathy and cardiomyopathy. Hum. Mol. Genet. *14*, 3079–3088.

60. Simons, C., Griffin, L.B., Helman, G., Golas, G., Pizzino, A., Bloom, M., Murphy, J.L., Crawford, J., Evans, S.H., Topper, S., et al. (2015). Loss-of-function alanyl-tRNA synthetase mutations cause an autosomal-recessive early-onset epileptic encephalopathy with persistent myelination defect. Am. J. Hum. Genet. *96*, 675–681.

61. Harel, T., Yesil, G., Bayram, Y., Coban-Akdemir, Z., Charng, W.L., Karaca, E., Al Asmari, A., Eldomery, M.K., Hunter, J.V., Jhangiani, S.N., et al.; Baylor-Hopkins Center for Mendelian Genomics (2016). Monoallelic and biallelic variants in *EMC1* identified in individuals with global developmental delay, hypotonia, scoliosis and cerebellar atrophy. Am. J. Hum. Genet. *98*, 562–570.

62. Rainger, J., Pehlivan, D., Johansson, S., Bengani, H., Sanchez-Pulido, L., Williamson, K.A., Ture, M., Barker, H., Rosendahl, K., Spranger, J., et al.; UK10K; Baylor-Hopkins Center for Mendelian Genomics (2014). Monoallelic and biallelic mutations in *MAB21L2* cause a spectrum of major eye malformations. Am. J. Hum. Genet. *94*, 915–923.

63. Chong, J.X., McMillin, M.J., Shively, K.M., Beck, A.E., Marvin, C.T., Armenteros, J.R., Buckingham, K.J., Nkinsi, N.T., Boyle, E.A., Berry, M.N., et al.; University of Washington Center for Mendelian Genomics (2015). De novo mutations in *NALCN* cause a syndrome characterized by congenital contractures of the limbs and face, hypotonia, and developmental delay. Am. J. Hum. Genet. *96*, 462–473.

64. Merle, N., Féraud, O., Gilquin, B., Hubstenberger, A., Kieffer-Jacquinot, S., Assard, N., Bennaceur-Griscelli, A., Honnorat, J., and Baudier, J. (2012). ATAD3B is a human embryonic stem cell specific mitochondrial protein, re-expressed in cancer cells, that functions as dominant negative for the ubiquitous ATAD3A. Mitochondrion *12*, 441–448.

65. Langer, T., Käser, M., Klanner, C., and Leonhard, K. (2001). AAA proteases of mitochondria: quality control of membrane proteins and regulatory functions during mitochondrial biogenesis. Biochem. Soc. Trans. *29*, 431–436.